Available online at www.sciencedirect.com

ScienceDirect

Geochimica et Cosmochimica Acta 213 (2017) 35–46

Geochimica et Cosmochimica Acta

www.elsevier.com/locate/gca

Iron and Zinc isotope fractionation during magmatism in the continental crust: Evidence from bimodal volcanic rocks from Hailar basin, NE China

Ying Xia, Shuangqing Li, Fang Huang *

CAS Key Laboratory of Crust–Mantle Materials and Environments, School of Earth and Space Sciences, USTC, Hefei 230026, China

Received 26 July 2016; accepted in revised form 12 June 2017; Available online 21 June 2017

Abstract

This study presents Fe–Zn isotope data for a suite of well–characterized bimodal volcanic rocks from Hailar Basin, northeast China to understand the mechanism of Fe isotope fractionation in highly differentiated igneous rocks. The samples range from basaltic trachyandesites to trachytes–rhyodacites, and rhyolites. The $\delta^{56}Fe$ values increase with increasing SiO_2 contents with the rhyolites having the highest $\delta^{56}Fe$ (up to $0.64 \pm 0.02‰$) among the previously reported data for igneous rocks at a similar SiO_2. The lack of correlation between $\delta^{56}Fe$ and Rb/La argues against the effect of fluid exsolution on Fe isotopes. The $\delta^{56}Fe$ do not show a clear correlation with $\delta^{66}Zn$ and radiogenic isotopes, suggesting that thermal diffusion or crustal contamination cannot produce the high $\delta^{56}Fe$ in Hailar volcanic rocks.

Fe isotopic variation in Hailar volcanic rocks can be explained by two steps of magmatism. During the first step, partial melting of basaltic trachyandesites with an average $\delta^{56}Fe$ of $0.09 \pm 0.14‰$ produced trachytes–rhyodacites with an average $\delta^{56}Fe$ of $0.24 \pm 0.27‰$. Modelling using rhyolite–MELTS shows that Fe isotopes can be fractionated by preferential partitioning of isotopically different Fe^{3+} and Fe^{2+} between the solid residue and partial melt. The second step involves formation of rhyolites with significantly high $\delta^{56}Fe$ through partial melting or extensive crystallization of crust materials, during which isotopically heavy Fe preferentially partition into the rhyolitic melt. Therefore, fractionation of Fe isotopes between melts and minerals can result in high $\delta^{56}Fe$ in SiO_2-rich igneous rocks and apparent Fe isotope heterogeneity within the continental crust.

Keywords: Fe isotopes; Zn isotopes; Bimodal volcanic rocks; Partial melting; Crystallization

1. INTRODUCTION

Iron is the most abundant redox–sensitive element in the terrestrial planets, as well as the Moon in the inner Solar System. It has three oxidation states (Fe^0, Fe^{2+}, and Fe^{3+}) that are partitioned between coexisting phases during redox-related geochemical processes, generating detectable Fe isotopic fractionation even at high temperature in the Earth's mantle. In the last decade, Fe isotopes have become a useful tool in exploring a number of fundamental high temperature geochemical processes, including core–mantle segregation (Poitrasson et al., 2009; Hin et al., 2012; Shahar et al., 2014), mantle melting and metasomatism (Williams et al., 2012), magma differentiation (Williams and Bizimis, 2014; Nebel et al., 2015), and ore–deposit formation (Wawryk and Foden, 2015).

One aspect of Fe isotopes that remains to be better understood is that high silica igneous rocks (>71 wt.% SiO_2) show dramatically higher $\delta^{56}Fe$ than those with mafic- to intermediate-compositions (e.g. Poitrasson and Freydier, 2005; Heimann et al., 2008; Foden et al., 2015; Schoenberg and von Blanckenburg, 2006; Schuessler

* Corresponding author.
E-mail address: fhuang@ustc.edu.cn (F. Huang).

http://dx.doi.org/10.1016/j.gca.2017.06.018
0016-7037/

et al., 2009; Sossi et al., 2012; Telus et al., 2012; Zambardi et al., 2014). Several hypotheses have been proposed to explain such signature, including fractional crystallization of isotopically light silicate minerals (Dauphas et al., 2014; Schoenberg and von Blanckenburg, 2006; Schuessler et al., 2007; Teng et al., 2008; Sossi et al., 2012), temperature gradient–driven diffusive differentiation (Lundstrom, 2009; Zambardi et al., 2014), and exsolution of Fe^{2+}–rich fluids (Poitrasson and Freydier, 2005; Heimann et al., 2008; Telus et al., 2012). Open–system mixing with an isotopically heavy exogenic assimilant was also proposed by Schoenberg and von Blanckenburg (2006), but such isotopically heavy material has not been identified. Therefore, there are various processes that have differing influences on the formation of silicic rocks. However, no single petrogenetic mechanism that can give rise to previously reported high δ^{56}Fe in Si–rich igneous rocks, hampering our understanding of Fe isotope fractionation mechanism in evolved igneous rocks and thus, application in magmatic differentiation processes of the continental crust.

Late Mesozoic bimodal volcanic rocks are widely exposed in the Hailar basin, NE China, which provides an excellent opportunity to study the effect of intra-crust magmatism on Fe isotope compositions of igneous rocks. These rocks have a wide range in chemical compositions from mafic (basaltic trachyandesites) to felsic (trachytes–rhyodacites and rhyolites) (Li et al., 2014). Systematic petro–geochemiscal studies suggest that mafic rocks were derived from melting of a subduction-modified mantle. Trachytes–rhyodacites originated from melting of juvenile crust with compositions similar to basaltic trachyandesite, due to heat released by underplating of mantle–derived magmas during lithospheric extension (Li et al., 2014), while rhyolites resulted from magmatic differentiation of juvenile crust materials with intermediate compositions.

To better understand the mechanism for Fe isotope fractionation in evolved igneous rocks, we present systematic Fe isotope data for the well–characterized bimodal volcanic rocks from the Hailar basin. Additionally, we measured Zn isotope ratios for the volcanic rocks to scrutinize other processes responsible for Fe isotope fractionation. Combining with major and trace element compositions, Fe and Zn isotope data and rhyolite-MELTs modelling help us decipher the processes that produce the high δ^{56}Fe in the SiO_2-rich igneous rocks.

2. GEOLOGICAL BACKGROUND AND SAMPLE SELECTION

After the accretion of the late Mesoproterozoic to Carboniferous Central Asian Orogenic Belt (CAOB) between the Siberian and North China cratons (NCC), late Mesozoic extension of the lithosphere in NE China produced a large basin–and–range setting in the CAOB and NCC (Ren et al., 2002). Crustal extension was accompanied by exhumation of metamorphic core complexes (Daoudene et al., 2009; Wang et al., 2011), formation of volcano–sedimentary basins (Ren et al., 2002; Li et al., 2012), and emplacement of voluminous mafic and felsic igneous rocks (Zhang et al., 2008a; Wu et al., 2011). The Hailar basin is in the northern part of the CAOB (Fig. 1a). Drill core samples (Fig. 1b) show that the basement of the Hailar basin comprises late metavolcano–sedimentary assemblages (ca. 360 to 295 Ma old) and intrusive granitoids (ca. 282 to 295 Ma old). The overlying strata consist of a volcanic sequence (~1 km thick) with mainly mafic rocks at the base and felsic rocks, minor intercalated basalts and non–marine sedimentary rocks (~3 km thick) on the top. Field observations and geochemical data of the extension–related igneous rocks illustrate the predominantly bimodal composition, consistent with observations from drilling core samples (Fan et al., 2003; Zhang et al., 2008b; Xu et al., 2013).

Thirteen basaltic trachyandesites (ca. 160 to 140 Ma), 7 trachytes–rhyodacites (ca. 132 Ma), and 9 rhyolites (ca. 125 Ma) were selected for Fe and Zn isotope analyses. The samples collected here represent the variety of lithologies described by drilling core (Fig. 1b) and field observation. U–Pb zircon ages, major and trace elements, Nd, Sr, and Pb isotope data of these samples have been reported in Li et al. (2014), providing evidence for involvement of a sedimentary component in the mantle source of mafic rocks. Trachytes-rhyodacites and rhyolites display overlapping radiogenic Sr, Nd, and Pb isotopes, but systematically distinct element geochemical features compared to basaltic trachyandesites. Two separate differentiation processes have been proposed to explain the geochemical variability in felsic rocks (Li et al., 2014):

i. The offset of elemental compositions (e.g. SiO_2, $Fe_2O_{3\ total}$, P, and Th concentrations) between trachytes–rhyodacites and the mafic rocks argue against continuous crystallization from mafic rocks to trachytes–rhyodacites. Instead, trachytes–rhyodacites are proposed to originate from partial melting of the juvenile mafic crust resembling the basaltic trachyandesites, triggered by heat from underplating of mantle-derived magmas.
ii. The most differentiated lithology in the Hailar basin, i.e. the rhyolites, have similar radiogenic Sr, Nd, and Pb isotopes, but younger zircon ages, higher Nb and Th contents, lower LREE/HREE relative to the trachytes–rhyodacites. These features suggest that the less differentiated juvenile crustal materials evolve to rhyolite with accessory minerals (e.g. apatite, titanite) controlling the LREE budgets.

3. ANALYTICAL METHODS

Fe and Zn isotope compositions of 29 samples were measured in the CAS Key Laboratory of Crust–Mantle Materials and Environments at the University of Science and Technology of China (USTC), Hefei, China. Sample powders containing ~50 μg Fe were digested in a 3:1 mixture of double–distilled concentrated HF/HNO_3 in Savillex beakers on a hotplate at ~100 °C. Samples were evaporated to dryness and repeatedly dissolved in aqua regia until complete dissolution was achieved. The purification procedures and analytical methods for Fe isotopes were adapted from those described in Huang et al. (2011). Briefly, anion

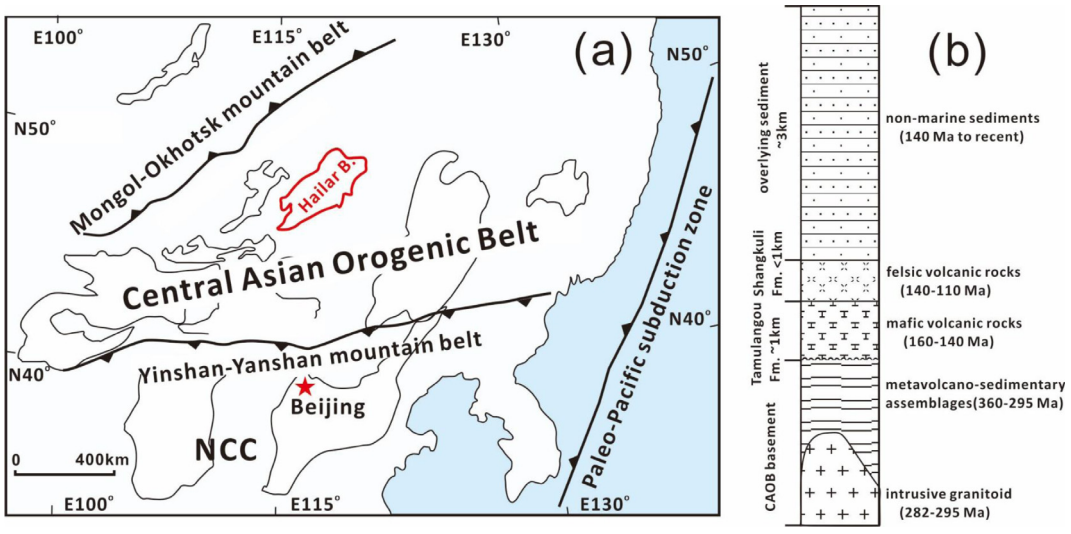

Fig. 1. Geological sketch map and simplified stratigraphic profile of the Hailar basin. (a) Haiar basin is situated in the Central Asian Orogenic Belt (CAOB). The Map is modified after Li et al. (2014). (b) Stratigraphic profile is simplified after Min-Na et al. (2013), and age data are from Li et al. (2014) and references therein. Abbreviations: NCC—North China Craton, Fm.—Formation.

exchange chromatography (AG1-X8, 200–400 mesh) using HCl were used to remove matrix elements from Fe. The recovery of Fe was >99.5%. Procedural Fe blanks were always <20 ng, negligible relative to the amount of Fe processed from the samples.

Purified Fe was analyzed using Thermo Scientific Neptune Plus MC–ICP–MS. Standard bracketing with IRMM-014 was used to correct instrumental mass bias. ^{53}Cr, ^{54}Fe, ^{56}Fe, ^{57}Fe, ^{58}Fe, and ^{60}Ni were measured in a static mode on the L3, L1, C, H1, H2, and H4 Faraday cups, respectively. Isotope ratios were analyzed at a high resolution mode with a resolving power of ~8000 (m/Δm with a 95% peak edge definition), allowing ^{56}Fe to be resolved from isobaric interferences. Isotopic data are reported using the delta (δ) notation,

$$\delta^{i}\mathrm{Fe} = [(^{i}\mathrm{Fe}/^{54}\mathrm{Fe})_{\mathrm{sample}} / (^{i}\mathrm{Fe}/^{54}\mathrm{Fe})_{\mathrm{IRMM-014}} - 1] \times 1000\,(‰),$$

where i refers to mass 56 or 57.

Sample powders containing ~2 μg Zn were digested for isotope measurement. The analytical method was adapted from Chen et al. (2016). After full digestion using a procedure similar to that of Fe isotope analysis described above, the samples were loaded in 6 M HCl on a column with 2 mL anion exchange resin (AG MP-1M, 100–200 mesh) to purify Zn from matrices. A second separation step with 0.5 mL AG MP–1M (100–200 mesh) resin was used for further purification. The yield of Zn was 99%. Total procedural blanks were <10 ng, also negligible relative to the total amount of Zn in the samples. Zinc isotopes were analyzed on the Neptune Plus MC–ICP–MS at low resolution. Solutions were introduced using a PFA microflow nebuliser with an uptake rate of 50 μL min^{-1}. Isotope ratios are expressed in δ–notation, relative to the Zn JMC–Lyon standard:

$$\delta^{j}\mathrm{Zn} = [(^{j}\mathrm{Zn}/^{64}\mathrm{Zn})_{\mathrm{sample}} / (^{j}\mathrm{Zn}/^{64}\mathrm{Zn})_{\mathrm{JMC-Lyon}} - 1] \times 1000\,(‰),$$

where j refers to mass 66 or 68.

Accuracy and precision of isotopic measurements were assessed by analyzing international whole rock standards, including BCR–1, AGV–2, RGM–1, and BHVO–2. The long-term external precisions of δ^{56}Fe and δ^{66}Zn are better than 0.05‰ (2SD). The measured standard values (Table 1) agree well with previously published data within error for both Fe isotopes (Rouxel et al., 2003) and Zn isotopes (Sossi et al., 2015; Chen et al., 2016). δ^{56}Fe and δ^{66}Zn of replicates are also consistent within error, demonstrating the reliability of our data.

4. RESULTS

Iron isotopic data are reported in Table 1 and plotted in Fig. 2. The δ^{56}Fe of the Hailar basaltic trachyandesites ranges from 0 ± 0.02‰ to 0.24 ± 0.04‰, with an average of 0.09 ± 0.14 (2SD, n = 13), while δ^{56}Fe for trachytes–rhyodacites range from 0.06 ± 0.05‰ to 0.41 ± 0.04‰ with an average of 0.24 ± 0.27‰ (2SD, n = 7). The rhyolites have δ^{56}Fe ranging from 0.20 ± 0.03‰ to 0.64 ± 0.02‰ (average of 0.40 ± 0.28‰, n = 9), the highest among the reported data for igneous rocks. Overall, Fe isotope data of basaltic trachyandesites vary in a limited range and overlap the value of average oceanic basalts (Dauphas et al., 2009). δ^{56}Fe in trachytes-rhyodacites and rhyolites show a striking variability, which increases with increasing SiO_2 and decreasing $Fe_2O_{3\ \mathrm{total}}$ contents, consistent with previous observations.

δ^{66}Zn values in basaltic trachyandesites show a limited variation (~0.1‰), whereas those in more differentiated lithologies, i.e. trachytes–rhyodacites, and rhyolites span a wide range of 0.24‰ (Table 1, Fig. 2b). δ^{66}Zn of the basaltic trachyandesites range from 0.19 ± 0.02‰ to 0.30 ± 0.01‰, with an average value of 0.27 ± 0.06‰ (2SD, n = 13), similar to the average oceanic basalts (e.g. 0.28 ± 0.05‰ in Chen et al. (2013)). δ^{66}Zn in trachytes–rhyodacites ranges from 0.24 ± 0.03‰ to 0.48 ± 0.02‰, with a mean of

Table 1
Iron and zinc isotopic compositions (‰) of the whole rock samples and geostandards.

Sample	$\delta^{56}Fe$	2SD	$\delta^{57}Fe$	2SD	n	Replicated analyses					$\delta^{66}Zn$	2SD	$\delta^{68}Zn$	2SD	n	Replicated analyses				
						$\delta^{56}Fe$	2SD	$\delta^{57}Fe$	2SD	n						$\delta^{66}Zn$	2SD	$\delta^{68}Zn$	2SD	n
Basaltic trachyandesites (average $\delta^{56}Fe$: 0.09 ± 0.14‰, $\delta^{66}Zn$: 0.27 ± 0.06‰)																				
FK10–98	0.18	0.03	0.24	0.06	3						0.30	0.03	0.59	0.04	3					
FK10–99	0.09	0.04	0.16	0.06	4						0.30	0.06	0.60	0.14	3					
FK10–96	0.24	0.02	0.36	0.04	4	0.24	0.04	0.33	0.09	3	0.21	0.00	0.42	0.02	3	0.19	0.02	0.37	0.00	3
FK10–97	0.08	0.02	0.15	0.20	4						0.27	0.03	0.55	0.08	3					
FK10–100	0.07	0.05	0.08	0.07	4						0.28	0.02	0.56	0.07	3					
FK10–101	0.05	0.02	0.09	0.06	4						0.30	0.03	0.61	0.03	3					
FK10–78	0.05	0.05	0.10	0.14	4						0.27	0.02	0.56	0.05	3					
FK10–79	0.18	0.06	0.28	0.08	4	0.14	0.01	0.22	0.10	3	0.26	0.03	0.53	0.03	3	0.26	0.01	0.53	0.02	3
FK10–77	0.05	0.03	0.11	0.10	4						0.29	0.03	0.58	0.08	3					
FK10–116	0.00	0.02	-0.01	0.08	4						0.26	0.05	0.53	0.11	3					
FK10–111	0.15	0.03	0.30	0.08	4						0.24	0.03	0.50	0.02	3					
FK10–112	0.04	0.05	0.06	0.09	4						0.25	0.01	0.49	0.01	3					
FK10–113	0.02	0.04	0.12	0.15	4						0.31	0.01	0.59	0.05	3					
Trachytes–rhyodacites (average $\delta^{56}Fe$: 0.24 ± 0.27‰, $\delta^{66}Zn$: 0.35 ± 0.14‰)																				
FK10–80	0.11	0.01	0.18	0.04	4						0.32	0.04	0.63	0.07	3					
FK10–81	0.36	0.03	0.59	0.06	4						0.36	0.02	0.72	0.07	3					
FK10–102	0.06	0.05	0.12	0.07	4						0.24	0.03	0.49	0.01	3					
FK10–104	0.33	0.03	0.47	0.06	4						0.48	0.02	0.95	0.04	3					
FK10–105	0.41	0.04	0.58	0.08	4						0.33	0.03	0.69	0.03	3	0.35	0.05	0.69	0.04	3
FK10–107	0.21	0.02	0.34	0.08	4						0.23	0.02	0.47	0.07	3					
FK10–108	0.16	0.03	0.22	0.04	4						0.34	0.13	0.72	0.26	3	0.35	0.02	0.74	0.03	3
Rhyolites (average $\delta^{56}Fe$: 0.40 ± 0.28‰, $\delta^{66}Zn$: 0.31 ± 0.13‰)																				
FK10–83	0.64	0.02	0.93	0.09	4	0.60	0.02	0.92	0.07	3	0.29	0.02	0.59	0.04	3	0.29	0.03	0.59	0.06	3
FK10–87	0.20	0.03	0.29	0.04	4						0.46	0.05	0.88	0.12	3	0.43	0.07	0.86	0.09	3
FK10–86	0.24	0.03	0.34	0.05	4						0.26	0.01	0.52	0.01	3					
FK10–88	0.47	0.04	0.57	0.28	4	0.48	0.04	0.68	0.04	3	0.26	0.04	0.50	0.06	3					
FK10–89	0.40	0.04	0.63	0.12	4						0.29	0.01	0.60	0.04	3					
FK10–90	0.37	0.02	0.56	0.12	4						0.27	0.02	0.63	0.02	3					
FK10–91	0.26	0.05	0.35	0.09	4						0.34	0.01	0.67	0.05	3					
FK10–84	0.50	0.05	0.77	0.07	4															
FK10–85	0.47	0.03	0.70	0.04	4						0.27	0.01	0.55	0.02	3					
Geostandards																				
BHVO–2	0.08	0.03	0.12	0.04	4	0.12	0.02	0.16	0.05	3	0.33	0.01	0.68	0.05	3					
BCR–1	0.09	0.04	0.14	0.08	4						0.27	0.03	0.55	0.07	3					
AGV–2	0.11	0.07	0.15	0.09	3						0.27	0.04	0.60	0.02	3					
RGM–1	0.22	0.05	0.30	0.03	3						0.35	0.05	0.72	0.09	3					

Note: Error bars on isotopic compositions are 95% confidence intervals.
* Replicated analyses are for newly digested samples.

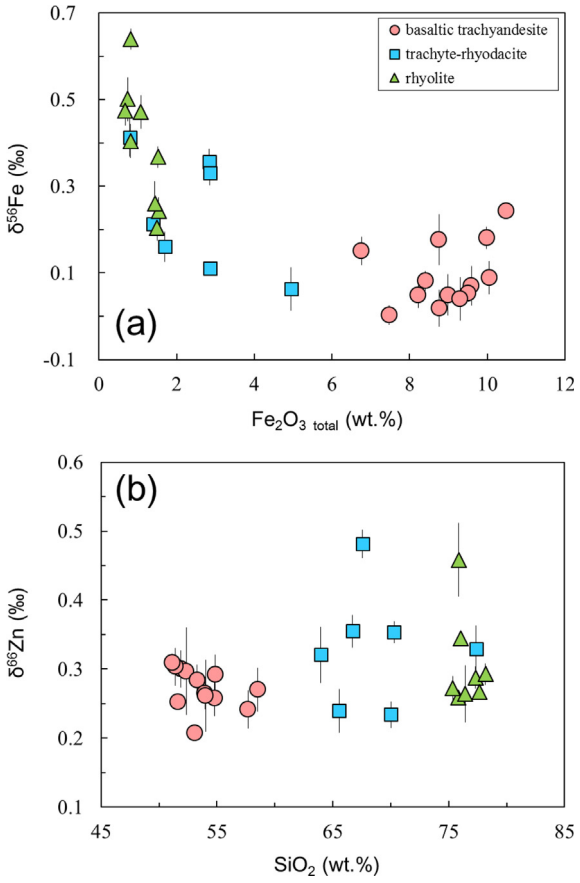

Fig. 2. (a) $\delta^{56}Fe$ vs. $Fe_2O_{3\ total}$, and (b) $\delta^{66}Zn$ vs. SiO_2 of Hailar volcanic rocks. $\delta^{56}Fe$ increases with decreasing Fe content, while $\delta^{66}Zn$ shows limited variations with SiO_2 content. Major element data are from Li et al. (2014).

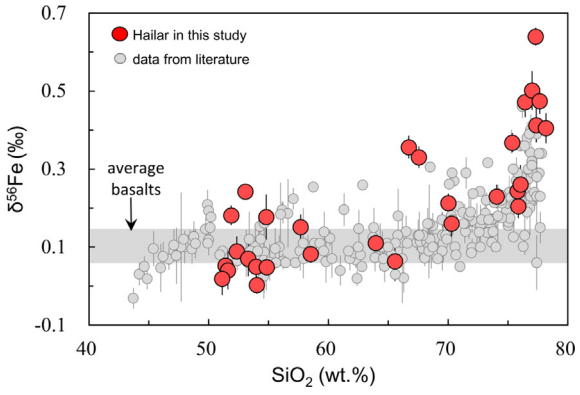

Fig. 3. $\delta^{56}Fe$ vs. SiO_2 of Hailar volcanic rocks comparing with plutonic and volcanic rocks from the literature. Red circles represent all samples from Hailar; Grey circles denote data compiled from literature (Dauphas et al., 2004); Poitrasson and Freydier, 2005; Heimann et al., 2008; Foden et al., 2015; Schuessler et al., 2009; Teng et al., 2008; Sossi et al., 2012; Telus et al., 2012; Zambardi et al., 2014). Uncertainties are 2 standard deviations of the mean (2SD). Heavy Fe isotopes are enriched in high silica igneous rocks, consistent with previous studies. The gray area represents the average oceanic basalts ($\delta^{56}Fe = 0.10‰$) with a 95% confidence interval (Dauphas et al., 2009).

$0.35 \pm 0.14‰$ (2SD, n = 7). $\delta^{66}Zn$ in rhyolites span a wide range from $0.26 \pm 0.01‰$ to $0.46 \pm 0.05‰$, with an average of $0.31 \pm 0.13‰$ (2SD, n = 8), identical to the averages of both basaltic trachyandesites and trachytes–rhyodacites within error. Collectively, there is no clear correlation between $\delta^{66}Zn$ and magma differentiation indices such as SiO_2 content (Fig. 2b).

5. MECHANISMS FOR FE ISOTOPE FRACTIONATION IN BIMODAL VOLCANIC ROCKS

In agreement with previous studies, the most evolved igneous rocks (i.e. rhyolites) in Hailar are enriched in heavy Fe isotopes. Notably, rhyolite samples have the highest $\delta^{56}Fe$ (up to $0.64 \pm 0.02‰$ at 77 wt.% SiO_2) among the previously reported data for igneous rocks at a given silica content (Fig. 3) (e.g. Poitrasson and Freydier, 2005; Heimann et al., 2008; Foden et al., 2015; Schoenberg and von Blanckenburg, 2006; Teng et al., 2008; Schuessler et al., 2009; Sossi et al., 2012; Telus et al., 2012; Zambardi et al., 2014). Interpretations of the origin of high $\delta^{56}Fe$ in differentiated igneous rocks include fluid exsolution (Heimann et al., 2008; Poitrasson et al., 2009; Telus et al., 2012), thermal diffusion (Huang et al., 2010; Zambardi et al., 2014), open–system mixing (Schoenberg and von Blanckenburg, 2006), fractional crystallization (Teng et al., 2008; Sossi et al., 2012; Foden et al., 2015), and partial melting (Telus et al., 2012). The following section attempts to examine the processes fractionating Fe isotopes in Hailar volcanic rocks.

5.1. Fluid exsolution

Exsolution of isotopically light fluids during melt ascent and evolution was suggested to explain the high $\delta^{56}Fe$ observed in some evolved magmas (Poitrasson and Freydier, 2005; Heimann et al., 2008; Telus et al., 2012). Fluid exsolution may occur in SiO_2–rich magmas, because H_2O solubility in magmas decreases with decreasing pressure or increasing polymerization of silicate melt (Wyllie, 1977; Holtz et al., 2001). This process can be assessed by Zn isotopes because they may be fractionated by aqueous fluid exsolution (Telus et al., 2012), but show only limited fractionation during crystallization (Chen et al., 2013). The $\delta^{66}Zn$ of Hailar rhyolites vary within a range of 0.2‰ (Fig. 2b), whereas $\delta^{66}Zn$ values in basaltic trachyandesites are rather homogenous. If fluids preferentially remove isotopically light Zn from the residual magma (Telus et al., 2012), rhyolite (FK10–87) with the highest $\delta^{66}Zn$ (0.46‰) would be more likely affected by fluid exsolution. However, FK10–87 has $\delta^{56}Fe$ of 0.2‰, a low value in the range of the measured $\delta^{56}Fe$ in rhyolites (Table 1).

In addition, as fluids are supposed to simultaneously modify Fe and Zn isotope compositions, a negative or positive correlation between $\delta^{66}Zn$ and $\delta^{56}Fe$ could be expected if fluid exsolution played a significant role, which is not observed in the Hailar rhyolites (Fig. 4b). Rb/La is further utilized to evaluate the role of fluid. Rb and La are highly incompatible in major minerals of rhyolite, including feldspar, biotite, quartz, and amphibole (https://earthref.org/

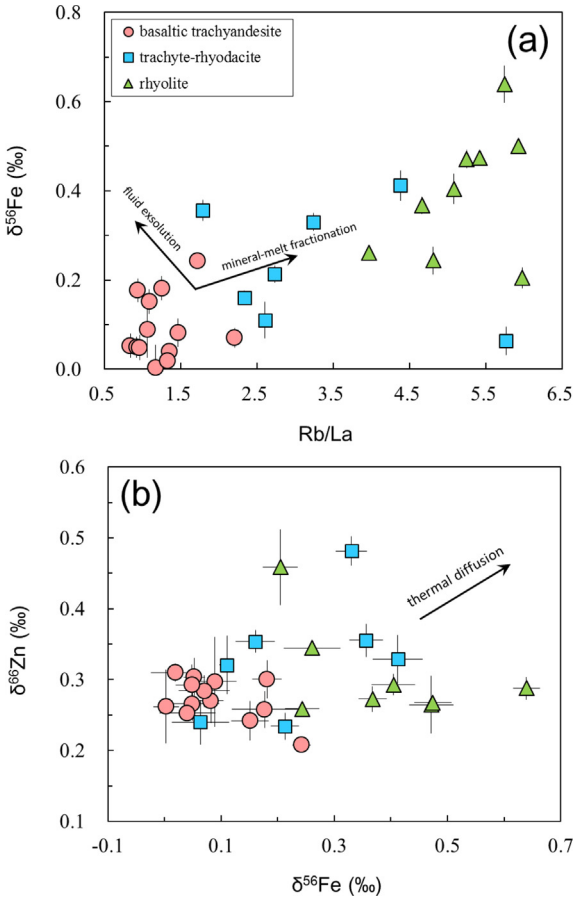

Fig. 4. (a) $\delta^{56}Fe$ vs. Rb/La ratio for Hailar volcanic rocks. Rb is fluid mobile while La is not. Rb is slightly more incompatible in major minerals than La. Fluid exsolution can reduce Rb/La and produce an apparent correlation between Rb/La and Fe isotope data, which is not observed in this study. (b) Variation of $\delta^{56}Fe$ with $\delta^{66}Zn$. The lack of a positive correlation between $\delta^{56}Fe$ and $\delta^{66}Zn$ demonstrates that thermal diffusion cannot explain the $\delta^{56}Fe$ in our samples.

KDD/), despite that Rb is slightly more incompatible than La. Thus Rb/La will not be apparently fractionated during crystallization and partial melting. Furthermore, because Rb is moderately fluid-mobile while La is not (Green (1994) and references therein), fluid exsolution may reduce Rb/La in the residual melt and thus produce a correlation between Rb/La and $\delta^{56}Fe$, which is, however, not observed in our data either (Fig. 4a). Hence, the high $\delta^{56}Fe$ in rhyolites could not result from fluid exsolution.

5.2. Thermal diffusion

Stable isotopes can be fractionated by thermal diffusion (e.g. Huang et al., 2009; Lundstrom, 2009; Richter et al., 2009a; Richter et al., 2009b; Huang et al., 2010; Lacks et al., 2012; Zambardi et al., 2014). Heavy isotopes are enriched at the cold end of a magmatic system along a temperature gradient, producing a positive correlation among different isotope systematics. According to Lacks et al. (2012), network formers are less fractionated than network modifiers during thermal diffusion. Given that Zn is a network modifier with similar relative mass differences of isotopes close to Fe isotopes, Zn isotopes are expected to be fractionated to a similar extent as Fe isotopes in thermal gradients, and thus result in a clear positive correlation between $\delta^{56}Fe$ and $\delta^{66}Zn$. However, no such a correlation between $\delta^{66}Zn$ and $\delta^{56}Fe$ is observed in Hailar samples (Fig. 4b), suggesting that volcanic rocks investigated here were not significantly influenced by thermal diffusion.

5.3. Crustal contamination

Exogenous crustal assimilation could also modify stable isotope signatures during magma differentiation. Schoenberg and von Blanckenburg (2006) attributed the positive correlation between $\delta^{56}Fe$ and SiO_2 content of the rocks from the Bergell intrusion in the Swiss Alps to open–system mixing of an isotopically heavy exogenic assimilant. For the Hailar samples investigated here, no apparent correlation between ε_{Nd} and Fe isotopes is observed. Furthermore, the average ε_{Nd} in rhyolites (+2.9) is slightly higher than basaltic trachyandesites (+1.3) and trachytes–rhyodacites (+2.2). If the ε_{Nd} reflects contamination of crustal materials (CAOB basement) which contain metavolcano–sedimentary assemblages with low ε_{Nd} (−6 to 0) (Li et al., 2014), then basaltic trachyandesites and trachytes–rhyodacites would have higher proportions of assimilants than rhyolites. However, basaltic trachyandesite and trachyte–rhyodacite samples generally exhibit consistent $\delta^{56}Fe$ with the global trend (Fig. 3). Furthermore, as Fe content of rhyolite is lower than basaltic trachyandesite and trachyte–rhyodacite, Fe isotope composition of rhyolite will be more sensitive to an isotopically distinct crustal contaminant. However, a correlation between $\delta^{56}Fe$ and ε_{Nd} in rhyolite is not observed. Therefore, evidences from Fe isotopes and radiogenic Nd isotopes argue against significant crustal contamination. One trachyte–rhyodacite (FK10-105) particularly has low ε_{Nd} (+0.1) and high $\delta^{56}Fe$ (0.41‰), which is potentially due to continental crust assimilation. However, assimilation of crustal components cannot explain the generally high $\delta^{56}Fe$ in Hailar rhyolites.

5.4. Iron isotopic fractionation between minerals and melts

After ruling out the possible processes discussed above, the variation of $\delta^{56}Fe$ in Hailar volcanic rocks is most likely explained by Fe isotope fractionation between melt and minerals during crystallization and partial melting. Crystallizing minerals with Fe isotope compositions distinguishable from the host magmas has been called on to explain Fe isotope compositions of igneous rocks (Teng et al., 2008; Sossi et al., 2012; Telus et al., 2012; Foden et al., 2015). Meanwhile, partial melting is generally recognized to be responsible for the ~0.1‰ shift of $\delta^{56}Fe$ in terrestrial basalts relative to peridotites and chondrites, due to equilibrium fractionation between Fe^{2+} and Fe^{3+} during redox melting (Dauphas et al., 2009, 2014). Accordingly, crustal melting which occurs at lower temperature and likely higher

Table 2
Rhyolite-MELTS modelling parameters adopted in this study.

Starting composition		Model	fO_2	Buffer	Open/closed	Pressure (kbar)	Initial T (°C)	Melt fraction at Initial T (wt.%)
SiO_2	51.41	①	−11.7	FMQ+3	Closed	2	780	19.9
TiO_2	1.93	②	−15.1	FMQ+0	Closed	2	760	8.0
Al_2O_3	16.61	③	−16.1	FMQ−1	Closed	2	760	9.2
Fe_2O_3total	9.51	④	−11.1	FMQ+2	Open	2	850	26.6
MnO	0.13	⑤	−12.1	FMQ+1	Open	2	850	23.8
MgO	5.08	⑥	−16.7	FMQ−3	Open	2	850	20.2
CaO	7.58							
Na_2O	3.79							
K_2O	1.78							
P_2O_5	0.69							
LOI (H_2O)	1.72							
Initial $\delta^{56}Fe$	0.15‰							

Note: Major elements data (wt.%) are from Li et al. (2014).
An intermediate $\delta^{56}Fe$ value of basaltic trachyandesite was chosen as initial $\delta^{56}Fe$.

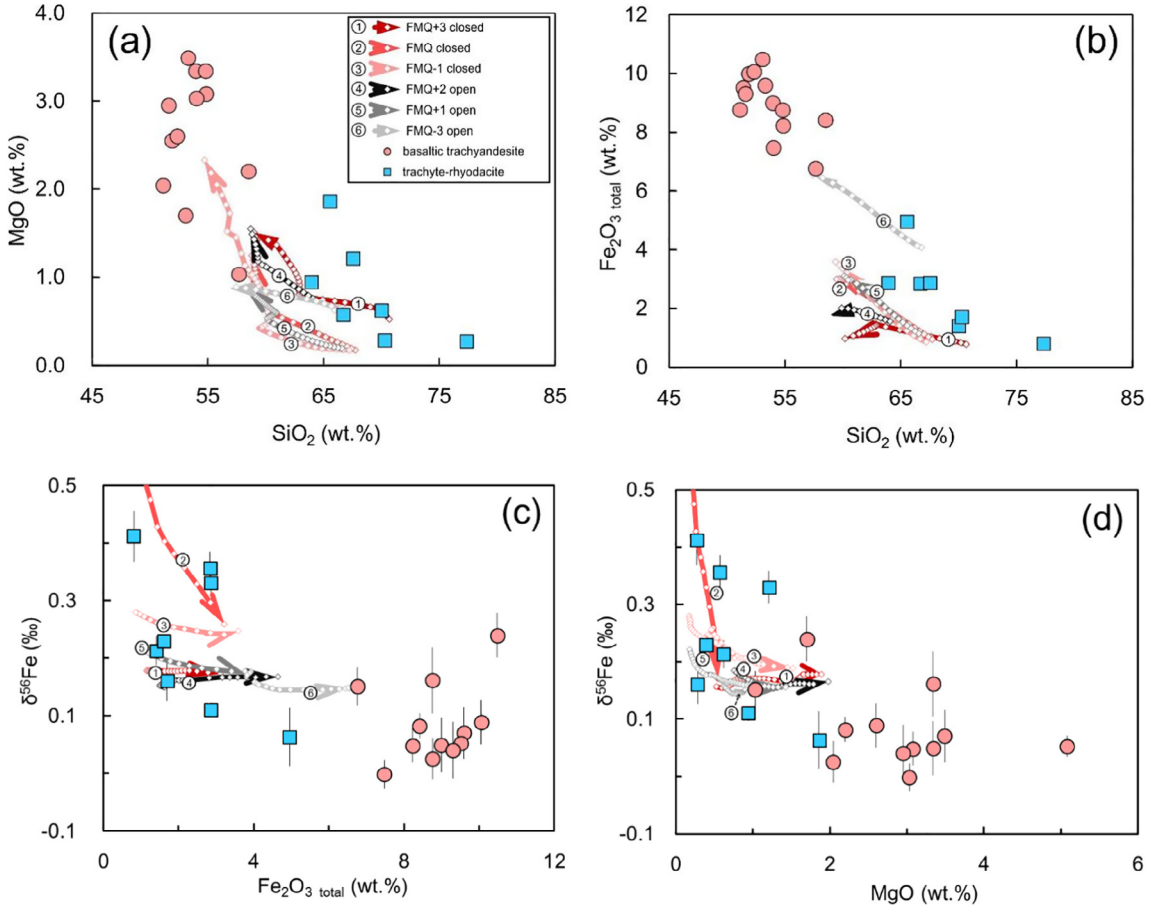

Fig. 5. Modelling major element and Fe isotope compositions of melts produced by partial melting of basaltic trachyandesite materials using the Rhyolite–MELTS software. The curves are the predicted correlations between (a) SiO_2 and MgO, (b) SiO_2 and $Fe_2O_{3\ total}$, (c) $\delta^{56}Fe$ and $Fe_2O_{3\ total}$, and (d) $\delta^{56}Fe$ and MgO under variable oxidation states. Diamond symbols on the curves represent melt produced at each step (8 °C/step) in the fractional melting modelling, and detailed information relevant to each step can be seen in Table S2. Parameters used in the model are shown in Table 2. The arrows indicate the order of melt extraction with increasing melting degree. At each step, isotopic fractionation factor between fractional melt and residual solid is calculated using the relevant force constant of Fe bond. As a first-order estimate, force constant data for silicate glasses (Dauphas et al., 2014) are taken to represent the melt. For melts with $SiO_2 < 70$ wt.%, force constants in less silicic glasses (i.e. 199 N/m for Fe^{2+} and 351 N/m for Fe^{3+}) are adopted. Force constants in solids are calculated using the weighted average value of the residual minerals (Jackson et al., 2009; Dauphas et al., 2014; Roskosz et al., 2015; Sossi and O'Neill, 2017).

oxygen fugacity (i.e. higher $Fe^{3+}/\sum Fe$) may fractionate Fe isotopes more than mantle melting. Telus et al. (2012) interpreted the systematically higher $\delta^{56}Fe$ (from 0.038‰ to 0.196‰) in leucosome relative to associated melanosome as crustal melting. Therefore, we scrutinize the role of crystallization and partial melting in fractionating Fe isotopes in the Hailar volcanic rocks.

5.4.1. Fe isotopes in basaltic trachyandesites

In the less differentiated samples, mafic minerals (e.g. olivine, pyroxene) are the major host of Fe, crystallization of which could be important in fractionating Fe isotopes. We evaluate the effect of this process based on major and trace element data. The low Mg–numbers (23 to 52), low Ni, Cr and Sc concentrations as well as small Eu–anomalies, suggest that the basaltic trachyandesites might have undergone extensive crystallization of olivine and clinopyroxene (Li et al., 2014). Therefore, crystallization is likely to be responsible for the variation of $\delta^{56}Fe$ (0‰ to 0.24‰) in basaltic trachyandesite samples (Fig. 2a). The obviously higher $\delta^{56}Fe$ in individual basaltic trachyandesite sample (e.g. FK10–96, 0.24 ± 0.02‰) than the mean oceanic basalts (~0.1‰) can be explained by early fractionation of isotopically light minerals (e.g. olivine) during mafic magmatic differentiation.

5.4.2. $\delta^{56}Fe$ of trachytes–rhyodacites and modelling using Rhyolite-MELTS

Trachytes–rhyodacites were produced by melting of the juvenile lower crustal lithologies with compositions similar to the basaltic trachyandesite samples (Li et al., 2014). To simulate the generation of trachytes–rhyodacites by fractional melting of basaltic trachyandesite material, the software Rhyolite–MELTS based on minimization of thermodynamic free energy was utilized (Gualda et al., 2012). We focused on the evolution of major elements and Fe isotope compositions of the partial melts, to reproduce the trend defined by trachyte–rhyodacite samples through modelling under varying conditions (Table 2). At each melting step, the program calculated the composition and mass of fractional melt and residual minerals. The melt was then instantaneously removed from the system. The least evolved basaltic trachyandesite (FK10–101) was chosen to represent the source of the trachytes–rhyodacites. The temperature increased from 760 °C to 1000 °C in an increment of 8 °C (Table 2), and pressure was fixed at 2 kbar. The evolution paths of the melt produced by fractional melting were modelled under varying fO_2 (~FMQ−3 to +3) in both closed and open systems to investigate how redox conditions affect the elemental and Fe isotopic compositions of the resulting melts.

To quantitatively examine Fe isotopic variation of the fractional melts when melting progresses, we used the force constant of Fe in melt and residual solid to obtain the equilibrium isotope fractionation factor. The weighted-average force constant of Fe bond in residual minerals was calculated based on the published data for minerals (Dauphas et al., 2009, 2014; Jackson et al., 2009; Roskosz et al., 2015; Sossi and O'Neill, 2017). Force constants of Fe^{3+} and Fe^{2+} end members in dacitic glass (Dauphas et al., 2014) were adopted to represent that of the trachyte–rhyodacite melt. The equilibrium Fe isotope fractionation factor ($\delta^{56}Fe_{melt-solid}$) was then calculated using Eq. (8) in Dauphas et al. (2014):

$$\delta^{56}Fe_{melt} - \delta^{56}Fe_{solid} = 2853 \times \frac{F_{melt} - F_{solid}}{T^2}, \quad (1)$$

where F is the force constant of Fe bond in either the melt or residual solid. The SiO_2 content and $\delta^{56}Fe$ of melts are plotted against MgO and $Fe_2O_{3\ total}$, as indices of partial melting in Fig. 5. As expected, the magnitude of the fractionation decreases with increasing temperature, but it is still significant at temperatures relevant to hydrous basaltic trachyandesite melting (e.g. ~0.4‰ at 750 °C). Overall, melts are enriched in Fe^{3+} and heavy Fe isotopes relative to their solid residues. $\delta^{56}Fe$ of melts produced in closed systems (model 1, 2, and 3 in Fig. 5) show a wider range, and they are systematically higher than those in open systems (model 4, 5, and 6 in Fig. 5). Comparison with open systems shows that closed systems cannot buffer fO_2 to keep $Fe^{3+}/\sum Fe$ of melts constant. As Fe^{3+} preferentially enters into melt, $Fe^{3+}/\sum Fe$ and the corresponding force constant in melt decreases with increasing melting degree. Thus, $\delta^{56}Fe$ of melts decreases with increasing melting degree, as coupled with major element compositions (e.g. Mg and Fe contents) (Fig. 5). In the open system, $Fe^{3+}/\sum Fe$ of melt is slightly higher or identical relative to the paired solid phases, resulting in slight or negligible variation in $\delta^{56}Fe$ of melt.

The whole–rock compositional trends of trachyte–rhyodacite can be simulated by fractional melting of basaltic trachyandesite within the model covered conditions. In specific, the models well reproduce the trend defined by major elements of the Hailar trachytes–rhyodacites at initially low fO_2 (i.e. model 6 in Fig. 5a, b). Most modelled results are low in Fe and Mg contents relative to the sample trend, likely ascribed to the chosen source (FK10-101) with lower Fe and Mg contents than the actual source. Meanwhile, the models well reproduce the trend defined by $\delta^{56}Fe$ and major contents at intermediate fO_2 (model 2 in Fig. 5c, d). Therefore, during partial melting of the mafic rocks, partitioning of Fe^{3+} and Fe^{2+} between felsic melts and mineral residues can produce higher $Fe^{3+}/\sum Fe$ in melt than the residual solid, producing higher mean Fe force constant in melts and thus higher $\delta^{56}Fe$ of trachytes–rhyodacites relative to their mafic sources.

5.4.3. Fe isotopes in rhyolites

Rhyolite samples possess almost similar Sr, Nd, and Pb isotopes to the less differentiated lithologies (i.e. basaltic trachyandesite and trachyte–rhyodacite), supporting an origin of the Hailar juvenile crust (Li et al., 2014). Because granite eutectic minimum yields melt with similar major elements to those produced by extensive crystallization (Ebadi and Johannes, 1991), both partial melting and extensive crystallization of intermediate materials can produce rhyolites (Scaillet et al., 2016). It is thus difficult to assign a certain magmatic process responsible for the major element compositions of Hailar rhyolites. The two processes cannot be clearly distinguished using trace element features either.

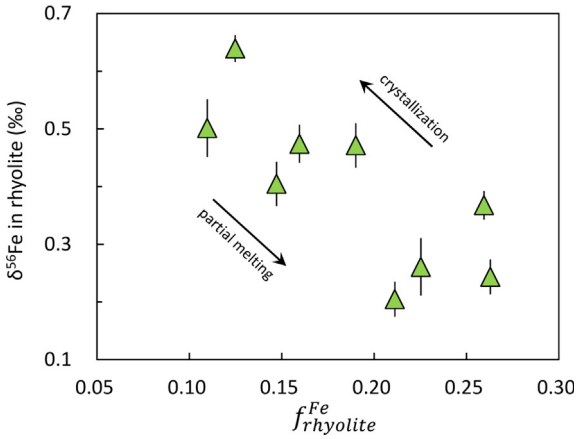

Fig. 6. δ^{56}Fe as a function of mass fraction of Fe in rhyolite ($f^{Fe}_{rhyoltie}$) after differentiation. $f^{Fe}_{rhyoltie}$ was calculated based on Th concentration in each rhyolite sample. Rhyolite can be considered as either partial melt during melting, or residual melt during crystallization. During both processes, isotopically heavy Fe prefer rhyolitic melt than minerals.

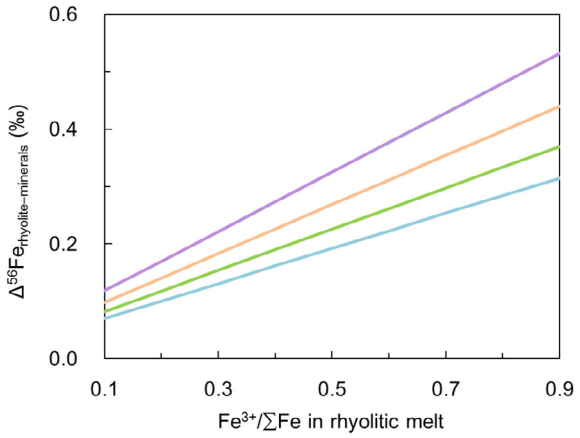

Fig. 7. Calculated $\delta^{56}Fe_{rhyolite\text{-}solid}$ as a function of $Fe^{3+}/\sum Fe$ in rhyolite and temperature. Once $Fe^{3+}/\sum Fe$ in source is fixed, $\delta^{56}Fe_{rhyolite\text{-}solid}$ decreases proportionally to $1/T^2$, and increases linearly with $Fe^{3+}/\sum Fe$ in rhyolite.

For example, La/Nb anomaly in rhyolite can be explained by apatite as a crystallization phase or alternatively a residual phase during melting. Therefore, we examine how equilibrium fractionation between rhyolitic melt and Fe-bearing minerals controls Fe isotope variations in both scenarios.

Identification of particular minerals responsible for the processes is not straightforward because: (i) δ^{56}Fe in Hailar rhyolites is not clearly correlated with crystallization indices such as $Fe_2O_{3\ total}$, SiO_2, and TiO_2 contents (Figs. 2a and 3), (ii) fractionation factors between Fe-bearing minerals stable in felsic rocks (e.g. biotite, amphibole, magnetite, ilmenite) and rhyolitic melt are almost not known, except that a fractionation factor between pyrrhotite and peralkaline rhyolite was calibrated by Schuessler et al. (2007). However, Fe isotope fractionation during rhyolitic melt-minerals equilibrium exchange can be assessed by plotting δ^{56}Fe in rhyolite versus degree of differentiation, e.g. $f^{Fe}_{rhyolite}$ or $f^{Fe}_{minerals}$ (mass fraction of Fe in either the rhyolitic melt or minerals after differentiation). The rhyolitic melt can be considered as either partial melt during melting, or residual melt during crystallization. $f^{Fe}_{minerals}$ can be expressed as:

$$f^{\mathrm{Fe}}_{minerals} = 1 - f^{\mathrm{Fe}}_{rhyolite} = 1 - \frac{f_{rhyolite} \times C^{\mathrm{Fe}}_{rhyolite}}{C^{\mathrm{Fe}}_{source}}, \quad (2)$$

where $C^{\mathrm{Fe}}_{rhyolite}$ and C^{Fe}_{source} are Fe content in the partial melt or residual melt and the source, respectively. $f_{rhyolite}$ is the mass fraction of rhyolitic melt, which can be calculated using a batch melting or equilibrium crystallization model:

$$C^{element}_{rhyolite} = \frac{C^{element}_{source}}{f_{rhyolite} + (1 - f_{rhyolite}) \times D}, \quad (3)$$

where $C^{element}$ is the concentration and D is partition coefficient of the element of interest. We assume that the rhyolite samples are derived from a less-evolved trachyte–rhyodacite material, e.g. FK10-81. Thus, C^{Fe}_{source} is 1.99 wt%, C^{Rb}_{source} is 127 ppm, and C^{Th}_{source} is 16 ppm (element data are from Li et al. (2014)). A minimum D close to zero is adopted for both Rb and Th on account of the extreme incompatibility (https://earthref.org/KDD/), which results in an approximation of $f_{rhyolite}$ which is equal to $C_{source}/C_{rhyolite}$ based on Eq. (3). The estimated $f_{rhyolite}$ using Rb and Th are almost identical (Table S3), demonstrating that our approximate calculation is reliable. Substituting the calculated$f_{rhyolite}$ into Eq. (2), $f^{Fe}_{minerals}$ corresponding to each rhyolite sample can be obtained, and then $f^{Fe}_{rhyolite}$ can be calculated (Table S3).

Calculated $f^{Fe}_{rhyolite}$ shows a negative correlation with δ^{56}Fe in rhyolites (Fig. 6), indicating that the Fe isotopic variation in rhyolites is associated with equilibrium partitioning of Fe between minerals and rhyolitic melt and thus degree of differentiation. In terms of partial melting, heavy Fe isotopes preferentially migrate from the source into melt, which results in rhyolite with low $f^{Fe}_{rhyolite}$ and high δ^{56}Fe. For the case of crystallization process, isotopically light Fe is preferentially partitioned into minerals, and δ^{56}Fe of the melt increases with decreasing $f^{Fe}_{rhyolite}$.

Both cases show that isotopically heavy Fe^{3+} prefers melt than minerals, consistent with the behavior of Fe isotopes during mantle melting (Dauphas et al., 2009). Fe isotopic variations in Hailar volcanic rocks further demonstrate that intra-crustal magmatism can produce Fe isotope fractionation larger than the ~0.1‰ shift of basalts from peridotites.

It is clear that the key factor controlling the direction and magnitude of Fe isotope fractionation is the integrated Fe isotope fractionation factor between rhyolitic melt and minerals ($\Delta^{56}Fe_{rhyolite-minerals}$). We have calculated the possible range of $\Delta^{56}Fe_{rhyolite-minerals}$ based on the force constant data (Dauphas et al., 2014) and Fe isotope mass balance relationship (Eq. (S1)). Collectively, $\Delta^{56}Fe_{rhyolite-minerals}$ is a function of F_{source}, $F_{rhyolite}$, $f^{Fe}_{rhyolite}$, and T (Appendix and Eq. (S9)). Force constants of Fe in rhyolitic and dacitic glasses are adopted from Dauphas et al. (2014) to represent

those in rhyolitic melt and source material with an intermediate composition, respectively. In each phase, the force constant of Fe is the weighted average force constant of Fe^{3+} and Fe^{2+}, thus a function of $Fe^{3+}/\sum Fe$. Force constants of Fe^{3+} and Fe^{2+} are 350 N/m and 207 N/m in dacite, and 385 N/m and 240 N/m in rhyolite, respectively (Dauphas et al., 2014). If all other parameters are fixed, an increment of $Fe^{3+}/\sum Fe$ by 0.1 in dacite source leads to a decrease of 0.05‰ of $\Delta^{56}Fe_{rhyolite-minerals}$ (Table S4), close to current analytical uncertainties. Assuming a dacite source under fO_2 near FMQ ($Fe^{3+}/\sum Fe = 0.1$) and $f^{Fe}_{rhyolite}$ is equal to the average of trachyte–rhyodacite samples (i.e. 0.2, Table S3), relationship between $\Delta^{56}Fe_{rhyolite-minerals}$ and $Fe^{3+}/\sum Fe$ in rhyolite at typical magma temperatures (1000–1300 K) can be described in Fig. 7. $\Delta^{56}Fe_{rhyolite-minerals}$ decreases proportionally to $1/T^2$, and increases linearly with $Fe^{3+}/\sum Fe$ in rhyolite at a given temperature.

Our results predict that equilibrium isotope fractionation between rhyolitic melt and minerals could dramatically elevate $\delta^{56}Fe$ of rhyolites. For the rhyolites in this study, application of the $\Delta^{56}Fe_{rhyolite-minerals}$ (Table S4) into batch melting and crystallization models can explain the range of $\delta^{56}Fe$ (0.20–0.64‰). For a fractional melting or crystallization process, Fe isotope fractionation between melt and mineral could be even larger. Therefore, the high $\delta^{56}Fe$ in Hailar rhyolites can be ascribed to removal of isotopically light Fe-bearing minerals from rhyolitic melt by partial melting, extensive crystallization, or a combination of both factors.

Because the upper and middle crust are dominated by differentiated products through partial melting and crystal fractionation (Rudnick and Gao, 2003), these processes are expected to produce striking Fe isotope heterogeneity within the continental crust. Furthermore, because Zn isotopes are barely fractionated during partial melting and crystallization (Chen et al., 2013), Zn isotopes can be used as potential tracers for deep carbonate cycling and fluid activities, in which cases isotopically distinct materials (e.g. marine carbonates and fluids) may be intensively involved (Liu et al., 2016; Pons et al., 2016).

6. CONCLUSIONS

This study reports Fe and Zn isotopic compositions of a suite of well–characterized basaltic trachyandesites, trachytes–rhyodacites, and rhyolites from the Hailar basin, NE China. The $\delta^{56}Fe$ for Hailar volcanic rocks are positively correlated with SiO_2 contents and inversely correlated with total Fe contents. Combined with the evidence from Zn isotopes, elemental and radiogenic isotope compositions (Li et al., 2014), we conclude that fluid exsolution, thermal diffusion, or exogenous crustal assimilation cannot explain the variations of $\delta^{56}Fe$ in Hailar volcanic rocks.

We attribute the variations of $\delta^{56}Fe$ in Hailar volcanic rocks to equilibrium isotope fractionation between melt and mineral during magmatism. Variations of $\delta^{56}Fe$ in basaltic trachyandesites result from extensive crystallization of olivine and clinopyroxene. Furthermore, melting of basaltic trachyandesite material is modelled using the rhyolite–MELTS at variable redox conditions. Simulated results suggest that major element and Fe isotope compositions of trachytes–rhyodacites can be explained by melting of basaltic trachyandesite material, during which Fe isotope fractionation between melt and residual solid is estimated based on available force constant data of Fe bonding. Finally, the high $\delta^{56}Fe$ in Hailar rhyolites are attributed to preferential partitioning of isotopically heavy Fe^{3+} into melt relative to minerals during partial melting or crystallization. Therefore, we conclude that intra-crustal magmatism can produce highly heterogeneous Fe isotopes in the continental crust.

ACKNOWLEDGEMENT

This work is supported by the DREAM Project of MOST China (2016YFC0600404), the National Science Foundation of China (41325011, 41573017), the Strategic Priority Research Program (B) of the Chinese Academy of Sciences (XDB18000000), and the 111 project. We deeply appreciate editorial handling by Shichun Huang and constructive comments from Paolo Sossi and two other anonymous reviewers who tremendously improved this manuscript. We are also grateful for discussion with Fukun Chen and Yongtai Yang.

APPENDIX A. SUPPLEMENTARY MATERIAL

Supplementary data associated with this article can be found, in the online version, at http://dx.doi.org/10.1016/j.gca.2017.06.018.

REFERENCES

Chen H., Nguyen B. M. and Moynier F. (2013) Zinc isotopic composition of iron meteorites: absence of isotopic anomalies and origin of the volatile element depletion. *Meteorit. Planet. Sci.* **48**, 2441–2450.

Chen S., Liu Y., Hu J., Zhang Z., Hou Z., Huang F. and Yu H. (2016) Zinc Isotopic Compositions of NIST SRM 683 and Whole-Rock Reference Materials. *Geostand. Geoanal. Res.*.

Daoudene Y., Gapais D., Ledru P., Cocherie A., Hocquet S. and Donskaya T. V. (2009) The Ereendavaa Range (north-eastern Mongolia): an additional argument for Mesozoic extension throughout eastern Asia. *Int. J. Earth Sci.* **98**, 1381–1393.

Dauphas N., Craddock P. R., Asimow P. D., Bennett V. C., Nutman A. P. and Ohnenstetter D. (2009) Iron isotopes may reveal the redox conditions of mantle melting from Archean to Present. *Earth Planet Sci. Letti* **288**, 255–267.

Dauphas N., Roskosz M., Alp E., Neuville D., Hu M., Sio C., Tissot F., Zhao J., Tissandier L. and Médard E. (2014) Magma redox and structural controls on iron isotope variations in Earth's mantle and crust. *Earth Planet Sc Lett* **398**, 127–140.

Dauphas N., van Zuilen M., Wadhwa M., Davis A. M., Marty B. and Janney P. E. (2004) Clues from Fe isotope variations on the origin of early Archean BIFs from Greenland. *Science* **306**, 2077–2080.

Ebadi A. and Johannes W. (1991) Beginning of melting and composition of first melts in the system Qz-Ab-Or-H2O-CO2. *Contrib. Miner. Petrol.* **106**, 286–295.

Fan W.-M., Guo F., Wang Y.-J. and Lin G. (2003) Late Mesozoic calc-alkaline volcanism of post-orogenic extension in the

northern Da Hinggan Mountains, northeastern China. *J. Volcanol. Geoth. Res.* **121**, 115–135.

Foden J., Sossi P. A. and Wawryk C. M. (2015) Fe isotopes and the contrasting petrogenesis of A-, I- and S-type granite. *Lithos* **212–215**, 32–44.

Green T. H. (1994) Experimental studies of trace-element partitioning applicable to igneous petrogenesis—Sedona 16 years later. *Chem. Geol.* **117**, 1–36.

Gualda G. A. R., Ghiorso M. S., Lemons R. V. and Carley T. L. (2012) Rhyolite-MELTS: a modified calibration of MELTS optimized for silica-rich, fluid-bearing magmatic systems. *J. Petrol.* **53**, 875–890.

Heimann A., Beard B. L. and Johnson C. M. (2008) The role of volatile exsolution and sub-solidus fluid/rock interactions in producing high ^{56}Fe ^{54}Fe ratios in siliceous igneous rocks. *Geochim. Cosmochim. Acta* **72**, 4379–4396.

Hin R. C., Schmidt M. W. and Bourdon B. (2012) Experimental evidence for the absence of iron isotope fractionation between metal and silicate liquids at 1GPa and 1250–1300 C and its cosmochemical consequences. *Geochim. Cosmochim. Acta* **93**, 164–181.

Holtz F., Johannes W., Tamic N. and Behrens H. (2001) Maximum and minimum water contents of granitic melts generated in the crust: a reevaluation and implications. *Lithos* **56**, 1–14.

Huang F., Chakraborty P., Lundstrom C., Holmden C., Glessner J., Kieffer S. and Lesher C. (2010) Isotope fractionation in silicate melts by thermal diffusion. *Nature* **464**, 396–400.

Huang F., Lundstrom C., Glessner J., Ianno A., Boudreau A., Li J., Ferré E., Marshak S. and DeFrates J. (2009) Chemical and isotopic fractionation of wet andesite in a temperature gradient: experiments and models suggesting a new mechanism of magma differentiation. *Geochim. Cosmochim. Acta* **73**, 729–749.

Huang F., Zhang Z., Lundstrom C. C. and Zhi X. (2011) Iron and magnesium isotopic compositions of peridotite xenoliths from Eastern China. *Geochim. Cosmochim. Acta* **75**, 3318–3334.

Jackson J. M., Hamecher E. A. and Sturhahn W. (2009) Nuclear resonant X-ray spectroscopy of (Mg, Fe) SiO_3 orthoenstatites. *Eur. J. Mineral.* **21**, 551–560.

Lacks D. J., Goel G., Bopp, IV, C. J., Van Orman J. A., Lesher C. E. and Lundstrom C. C. (2012) Isotope fractionation by thermal diffusion in silicate melts. *Phys. Rev. Lett.* **108**, 065901.

Li S.-Q., Chen F., Siebel W., Wu J.-D., Zhu X.-Y., Shan X.-L. and Sun X.-M. (2012) Late Mesozoic tectonic evolution of the Songliao basin, NE China: evidence from detrital zircon ages and Sr–Nd isotopes. *Gondwana Res.* **22**, 943–955.

Li S.-Q., Hegner E., Yang Y.-Z., Wu J.-D. and Chen F. (2014) Age constraints on late Mesozoic lithospheric extension and origin of bimodal volcanic rocks from the Hailar basin, NE China. *Lithos* **190–191**, 204–219.

Liu S.-A., Wang Z.-Z., Li S.-G., Huang J. and Yang W. (2016) Zinc isotope evidence for a large-scale carbonated mantle beneath eastern China. *Earth Planet Sci. Lett.* **444**, 169–178.

Lundstrom C. (2009) Hypothesis for the origin of convergent margin granitoids and Earth's continental crust by thermal migration zone refining. *Geochim. Cosmochim. Acta* **73**, 5709–5729.

Min-Na A., Zhang F.-Q., Yang S.-F., Chen H.-L., Batt G. E., Sun M.-D., Meng Q.-A., Zhu D.-F., Cao R.-C. and Li J.-S. (2013) Early Cretaceous provenance change in the southern Hailar Basin, northeastern China and its implication for basin evolution. *Cretac. Res.* **40**, 21–42.

Nebel O., Sossi P. A., Bénard A., Wille M., Vroon P. Z. and Arculus R. J. (2015) Redox-variability and controls in subduction zones from an iron-isotope perspective. *Earth Planet Sci. Lett.* **432**, 142–151.

Poitrasson F. and Freydier R. (2005) Heavy iron isotope composition of granites determined by high resolution MC-ICP-MS. *Chem. Geol.* **222**, 132–147.

Poitrasson F., Roskosz M. and Corgne A. (2009) No iron isotope fractionation between molten alloys and silicate melt to 2000 C and 7.7 GPa: Experimental evidence and implications for planetary differentiation and accretion. *Earth Planet Sci. Lett.* **278**, 376–385.

Pons M.-L., Debret B., Bouilhol P., Delacour A. and Williams H. (2016) Zinc isotope evidence for sulfate-rich fluid transfer across subduction zones. *Nature Commun.* **7**, 13794.

Ren J., Tamaki K., Li S. and Junxia Z. (2002) Late Mesozoic and Cenozoic rifting and its dynamic setting in Eastern China and adjacent areas. *Tectonophysics* **344**, 175–205.

Richter F. M., Dauphas N. and Teng F.-Z. (2009a) Non-traditional fractionation of non-traditional isotopes: evaporation, chemical diffusion and Soret diffusion. *Chem. Geol.* **258**, 92–103.

Richter F. M., Watson E. B., Mendybaev R., Dauphas N., Georg B., Watkins J. and Valley J. (2009b) Isotopic fractionation of the major elements of molten basalt by chemical and thermal diffusion. *Geochim. Cosmochim. Acta* **73**, 4250–4263.

Roskosz M., Sio C. K. I., Dauphas N., Bi W., Tissot F. L. H., Hu M. Y., Zhao J. and Alp E. E. (2015) Spinel–olivine–pyroxene equilibrium iron isotopic fractionation and applications to natural peridotites. *Geochim. Cosmochim. Acta* **169**, 184–199.

Rouxel O., Dobbek N., Ludden J. and Fouquet Y. (2003) Iron isotope fractionation during oceanic crust alteration. *Chem. Geol.* **202**, 155–182.

Rudnick R. and Gao S. (2003) Composition of the continental crust. *Treatise Geochem.* **3**, 659.

Scaillet B., Holtz F. and Pichavant M. (2016) Experimental constraints on the formation of silicic magmas. *Elements* **12**, 109–114.

Schoenberg R. and von Blanckenburg (2006) Modes of planetary-scale Fe isotope fractionation. *Earth Planet Sci. Lett.* **252**, 342–359.

Schuessler J. A., Schoenberg R., Behrens H. and von Blanckenburg F. (2007) The experimental calibration of the iron isotope fractionation factor between pyrrhotite and peralkaline rhyolitic melt. *Geochim. Cosmochim. Acta* **71**, 417–433.

Schuessler J. A., Schoenberg R. and Sigmarsson O. (2009) Iron and lithium isotope systematics of the Hekla volcano, Iceland—evidence for Fe isotope fractionation during magma differentiation. *Chem. Geol.* **258**, 78–91.

Shahar A., Hillgren V., Horan M., Mesa-Garcia J., Kaufman L. and Mock T. (2014) Sulfur-controlled iron isotope fractionation experiments of core formation in planetary bodies. *Geochim. Cosmochim. Acta*.

Sossi P. A., Foden J. D. and Halverson G. P. (2012) Redox-controlled iron isotope fractionation during magmatic differentiation: an example from the Red Hill intrusion, S. Tasmania. *Contrib. Mineral. Petrol.* **164**, 757–772.

Sossi P. A., Halverson G. P., Nebel O. and Eggins S. M. (2015) Combined separation of Cu, Fe and Zn from rock matrices and improved analytical protocols for stable isotope determination. *Geostand. Geoanal. Res.* **39**, 129–149.

Sossi P. A. and O'Neill H. S. C. (2017) The effect of bonding environment on iron isotope fractionation between minerals at high temperature. *Geochim. Cosmochim. Acta* **196**, 121–143.

Telus M., Dauphas N., Moynier F., Tissot F. L., Teng F.-Z., Nabelek P. I., Craddock P. R. and Groat L. A. (2012) Iron, zinc, magnesium and uranium isotopic fractionation during continental crust differentiation: the tale from migmatites, granitoids, and pegmatites. *Geochim. Cosmochim. Acta* **97**, 247–265.

Teng F.-Z., Dauphas N. and Helz R. T. (2008) Iron isotope fractionation during magmatic differentiation in Kilauea Iki lava lake. *Science* **320**, 1620–1622.

Wang T., Zheng Y., Zhang J., Zeng L., Donskaya T., Guo L. and Li J. (2011) Pattern and kinematic polarity of late Mesozoic extension in continental NE Asia: perspectives from metamorphic core complexes. *Tectonics* **30**.

Wawryk C. M. and Foden J. D. (2015) Fe-isotope fractionation in magmatic-hydrothermal mineral deposits: a case study from the Renison Sn–W deposit, Tasmania. *Geochim. Cosmochim. Acta* **150**, 285–298.

Williams H. M. and Bizimis M. (2014) Iron isotope tracing of mantle heterogeneity within the source regions of oceanic basalts. *Earth Planet Sci. Lett.* **404**, 396–407.

Williams H. M., Wood B. J., Wade J., Frost D. J. and Tuff J. (2012) Isotopic evidence for internal oxidation of the Earth's mantle during accretion. *Earth Planet Sci. Lett.* **321**, 54–63.

Wu F.-Y., Sun D.-Y., Ge W.-C., Zhang Y.-B., Grant M. L., Wilde S. A. and Jahn B.-M. (2011) Geochronology of the Phanerozoic granitoids in northeastern China. *J. Asian Earth Sci.* **41**, 1–30.

Wyllie P. J. (1977) Crustal anatexis: an experimental review. *Tectonophysics* **43**, 41–71.

Xu W.-L., Pei F.-P., Wang F., Meng E., Ji W.-Q., Yang D.-B. and Wang W. (2013) Spatial–temporal relationships of Mesozoic volcanic rocks in NE China: constraints on tectonic overprinting and transformations between multiple tectonic regimes. *J. Asian Earth Sci.* **74**, 167–193.

Zambardi T., Lundstrom C. C., Li X. and McCurry M. (2014) Fe and Si isotope variations at Cedar Butte volcano; insight into magmatic differentiation. *Earth Planet Sci. Lett.* **405**, 169–179.

Zhang J.-H., Ge W.-C., Wu F.-Y., Wilde S. A., Yang J.-H. and Liu X.-M. (2008a) Large-scale Early Cretaceous volcanic events in the northern Great Xing'an Range, northeastern China. *Lithos* **102**, 138–157.

Zhang L.-C., Zhou X.-H., Ying J.-F., Wang F., Guo F., Wan B. and Chen Z.-G. (2008b) Geochemistry and Sr–Nd–Pb–Hf isotopes of Early Cretaceous basalts from the Great Xinggan Range, NE China: implications for their origin and mantle source characteristics. *Chem. Geol.* **256**, 12–23.

Associate Editor: Shichun Huang